Mechanical Analysis of Fault Slip Rate Sites within the San Gorgonio Pass Region, Southern California USA

J. Hatch[1], M. Cooke[1,*], and H. Elston[1]

[1]Department of Earth, Geographic and Climate Sciences, University of Massachusetts, Amherst, USA
[*]Corresponding author:

This is a non-peer reviewer preprint that was submitted to Tektonkia on January 22, 2023. Please note that subsequent versions of this manuscript may have slightly different content. If accepted, the final version of this manuscript will be available via the Peer-reviewed Publication DOI link on the right hand side of this web page.

Author ORCIDs, email and twitter handle

A. Jennifer Hatch: 0000-0001-8877-2176 | jennbeyer6@gmail.com
B. Michele Cooke: 0000-0002-4407-9676 | cooke@umass.edu | @geomechCooke
C. Hanna Elston: 0000-0002-2420-5241 | helston@umass.edu | @HannaElston

Author contributions

Conceptualization: J. Hatch, M. Cooke
Formal Analysis: J. Hatch, M Cooke, H. Elston
Writing – original draft: J. Hatch, M. Cooke
Writing – review & editing: M. Cooke, J. Hatch, H. Elston

Abstract

Crustal deformation models show incompatibility between inferred fault geometry and geologic slip rates where model and geologic slip rates disagree. We do not know if the impact of these incompatibilities is local to sites or has wider effect on the fault system deformation. Here, we investigate the roles of structural position of sites and uncertainty of slip rates using one suite of mechanical models that limits the dextral slip rates to within the range of observed slip rates at the sites of geologic investigations and another suite that explores the impact of each slip rate site on each other and on the nearby fault system. The suites of models employ two viable configurations for the southern San Andreas fault: with and without an active northern slip pathway around the San Gorgonio Pass. The *Active Northern Pathway* model has slighter greater mismatch to young geologic slip rates than the *Inactive Northern Pathway* model but both are plausible. The impact of strike-slip rate sites on the system depends on their structural positions. Sites along short and segmented faults may have lesser impact on the system than either sites along longer faults or sites at fault branches. Consequently, inaccuracies in the slip rates used for seismic hazard assessment may have differing impacts depending on location of the slip rates. Fault branches along strike-slip faults warrant detailed investigation because these areas have high spatial variability of slip rate and accrue nearby off-fault deformation, affecting our ability to accurately assess seismic hazard of the region.

Non-technical summary

Earthquake hazard assessments rely on observations from the field and geophysical data that provide fault slip rate estimates at specific sites and inform active fault shape within the crust; however, uncertainty remains for both slip rate and shape. Numerical models that simulate slip along 3D faults of the southern San Andreas fault system produce slip rates that match some but not all field observations. At the mismatched sites, the model fault shape is incompatible with slip rates indicating inaccuracies in the fault shape and/or slip rate. We investigate how uncertainty or inaccuracy of a slip rate at one site impacts other sites and the overall fault system. Sites that are nearby each other have the greatest impact on each other and sites along fault branches have high impact on the fault system. This means that uncertainties in slip rates used for earthquake hazard assessment may have differing impacts depending on the slip rate site's location within the fault network. Hazard assessments can benefit from additional data along fault branches. Continuing to measure how fast faults are slipping in the field and reduce the uncertainty of such measurements will increase the accuracy of earthquake hazard assessments.

1. Introduction

Geologic evidence for slip rates along active faults provides critical information for constraining seismic hazards (e.g., Field et al., 2015; Morell et al., 2020)). Slip rate uncertainties that derive from a variety of sources can be large enough (>10 mm/yr) to compromise the accuracy of our hazard estimates. In the face of large uncertainties, collecting slip rate data from additional sites provides one way to improve constraints on active slip partitioning. However, in regions of multiple active faults with complex evolving geometry, where slip rates can vary both in space and in time (e.g., Elston et al., 2022; McGill et al., 2021; Zinke et al., 2017), this approach can yield slip rates that are inconsistent with each other. One such region is where the southern San

Andreas fault in southern California forms a restraining bend in the San Gorgonio Pass region (SGPr) (Figure 1). Because earthquakes along the San Andreas pose a great risk to the highly populated cities of southern California, the region has been the focus of many geologic investigations, and we have a lot of slip rate information on the San Andreas fault through the SGPr (Figure 1). However, the geologic slip rate information to date does not present a consistent interpretation of slip rate distribution along the strands and segments of the San Andreas fault.

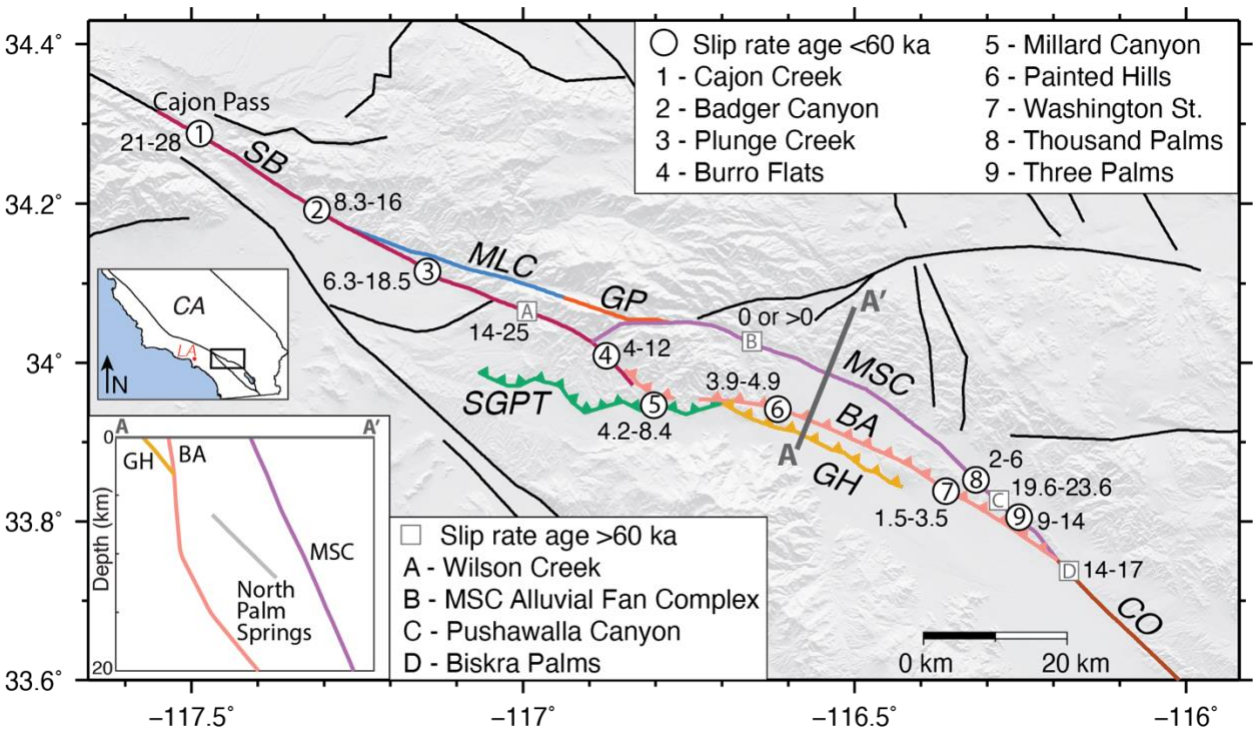

Figure 1. The surface traces of modeled faults overlain on a digital elevation map (DEM). Different trace colors indicate the specific fault segments. Numbers in circles show the location of slip rate sites that we use to constrain the model slip rate. Letters in squares the location of slip rate sites that we do not use to constrain the model slip rate. The bottom left inset shows the cross-section profile along the A-A' line (dark gray). The top left inset shows the region of interest (black rectangle) on a map of southern California. Table 1 lists the name and citation for all the slip rate sites. BA – Banning, CO – Coachella, GH – Garnet Hill, GP – Galena Peak, MLC – Mill Creek, MSC – Mission Creek, SB – San Bernardino, SGPT – San Gorgonio Pass Thrust.

For example, debate persists on the relative activity of the Mill Creek and Mission Creek strands, which provide a northern path for rupture through the SGPr (Figure 2; Blisniuk et al., 2021; Fosdick & Blisniuk, 2018; P. O. Gold et al., 2015; Kendrick et al., 2015). Kendrick et al. (2015) used reconstructed drainage segments across the Mill and Mission Creek strands (site B in Figure 1) to show that both strands, while active in the past, have been inactive for ~ 100 ka. However, a provenance study in this same area by Fosdick and Blisniuk (2018) suggests that these strands are currently active. Farther to the east along the Mission Creek fault, two sites within 5 km of each other (sites C and 9; Figure 1) have slip rates that differ by >10 mm/yr; 19.6 - 23.6 mm/yr at site C (Blisniuk et al., 2021) and 10-14 mm/yr at site 9 (Muñoz Zapata, 2017). In this case,

having abundant data increases our uncertainty about fault activity of the southern San Andreas fault because the rates are inconsistent; this is similar to having several clocks tell you different times.

Crustal deformation models provide a powerful tool for testing the mechanical consistency of slip along complex faults. We can test plausible fault configurations by comparing results of alternative mechanical models with geologic slip rates, uplift, and/or geodetic data (e.g., Beyer et al., 2018; Cooke & Dair, 2011; Fattaruso et al., 2014; Justin W. Herbert & Cooke, 2012). For example, Beyer et al. (2018) find that two among six plausible configurations of the San Andreas fault through the SGPr fit well the available geologic slip rates. Crustal deformation models can also highlight regions that would benefit from further investigation. Kinematic compatibility of a fault system describes how deformation is partitioned through the system (Gabrielov et al., 1996; Hatem et al., 2015), and its analysis can highlight regions where long-term fault slip rates are incompatible with fault geometry. If interpreted fault geometries and slip rates are kinematically incompatible, such as fast slip rates through a sharp fault bend, deformation that cannot be effectively accommodated as fault slip results in local off-fault deformation that impacts the fault slip budget. Because slip along faults may not sum to the regional loading in these regions of high incompatibility, we require additional data to better characterize partitioning of active deformation.

The abundant slip rate data along the geometrically complex southern San Andreas fault (Fig. 1) provides an ideal scenario to assess the relative impact of different slip rate sites on the partitioning of slip along the fault system. While some fault irregularities may only produce local off-fault deformation and persist throughout fault evolution (Hatem et al., 2017), other incompatibilities between fault geometry and slip rate may have great impact on slip rates throughout the fault system and promote reorganization of the fault system (e.g., Cooke et al., 2020; Fattaruso et al., 2016). By assessing the locations along the fault system with the greatest influence on slip rates, we can better understand the potential impact of uncertainties and inaccuracy on our seismic hazard estimates.

In this study, we use three-dimensional Boundary Element Method models that simulate deformation over many earthquake cycles to investigate the compatibility of interpreted fault geometry with interpreted slip rates through the SGPr (Figure 1). Rather than letting faults slip in response to tectonic loading as done with many previous models (e.g., Beyer et al., 2018), here we prescribe geologic slip rates at the sites of the investigation. This allows the models to incorporate both interpreted slip rates and fault geometry at the same time so that we can assess their compatibility. To explore the impact of these locations and slip rate uncertainties, we investigate a second suite of models that apply 1 mm/yr to each of the sites independently to assess how slip at different slip rate sites impact slip on the fault system due to variations in their structural position.

2. Geometry and slip rates of the southern San Andreas fault

Within the San Gorgonio Pass region (SGPr), the southern San Andreas fault forms a left-stepping restraining bend and becomes geometrically complex, with multiple active fault strands and a complex slip history (Figure 1; e.g., Matti et al., 1985; Matti & Morton, 1993). In this section, we describe the interpreted geometry and records of recent slip rate along both the southern and northern strands of the San Andreas fault (Table 1). The San Andreas fault geometry used in this study primarily follows that of the Southern California Earthquake Center Community Fault Model (CFM) v. 5 (Plesch, Shaw, & Kronman, 2007; Shaw et al., 2015) with exceptions noted below.

Dextral slip rates consistently decrease from north to south along the San Bernardino strand of the San Andreas fault from Cajon pass to where the strand approaches the San Gorgonio Pass thrust. Near Cajon Pass, at Cajon Creek the San Bernardino strand shows 21-28 mm/yr slip from ~14 ka geomorphic features (site 1: Weldon & Sieh, 1985). The next three sites to the south constrain slip rates from offsets of 10-16 ka alluvial fans with 8.3-16 mm/yr at Badger Canyon (site 2; McGill et al., 2021), 7-17 mm/yr dextral slip at Plunge Creek (site 3; McGill et al., 2013) and 14-25 mm/yr at Wilson Creek (site A: Harden & Matti, 1989). The fan age at Wilson Creek site is an estimate rather than a measurement, which results in a large slip rate range. Note: sites with slip rates that are either not well constrained or older than 16 ky are given a letter site name rather than a number and are not used to constrain the models. The southernmost slip rate site on the San Bernardino strand has 4-12 mm/yr slip rate recorded by offset of a ~4 ka alluvial fan at Burro Flats (site 4: Orozco, 2004).

Active slip along the southern pathway of the San Andreas fault within the SGPr occurs along the San Gorgonio Pass thrust, Garnet Hill strand, and Banning strand (Figure 1). The San Gorgonio Pass thrust is a north-dipping thrust fault that intersects the Earth's surface with a scalloped trace (e.g., Matti & Morton, 1993; Matti et al., 1985; Yule & Sieh, 2003). The San Gorgonio Pass thrust has offset ~8ka terraces to record a dextral-oblique slip rate of $5.7^{+2.7}/_{-1.5}$ mm/yr at Millard Canyon (site 5: Heermance & Yule, 2017). This net slip rate resolves to $5.2^{+2.4}/_{-1.4}$ mm/yr dextral slip and $2.4^{+1.1}/_{-0.6}$ of reverse slip To the east of Millard Canyon, the north-dipping Garnet Hill and Banning strands are nearly parallel in strike and have several different interpreted subsurface geometries (Fuis et al., 2017; Plesch, Shaw, Benson, et al., 2007; Yule & Sieh, 2003). For this study, we follow the interpretations of Fuis et al. (2017) that the Garnet Hill strand is only active in the footwall of the Banning strand (Figure 1). While the Garnet Hill strand does not offer geomorphic features that can provide slip rate estimates, the parallel Banning strand offsets ~6 ka alluvial fans at both its western and eastern ends. The fan at Painted Hills records 3.9-4.9 mm/yr dextral slip (site 6: Gold et al., 2015) and the fan at Washington Street, near the intersection of the Banning strand with Mission Creek strand, records 1.5-3.5 mm/yr dextral slip (site 7: Blisniuk et al., 2021).

The northern slip pathway of the San Andreas fault consists of the Mill Creek, Galena Peak, and Mission Creek strands (Figure 1). While the northern pathway was active in the past and served

as the primary structure of the San Andreas fault in this region, recent activity of these vertical faults are under debate (e.g., Beyer et al., 2018; Blisniuk et al., 2021; Fosdick & Blisniuk, 2018; Kendrick et al., 2015). Here, we include the Galena Peak strand as part of the northern pathway as it connects the Mill Creek strand and western part of the Mission Creek strand (e.g., Dibblee, 1964; Kendrick et al., 2015; Matti & Morton, 1993). This active fault configuration allows slip to by-pass Upper Raywood Flats where Kendrick et al. (2015) see no evidence of slip in the past 100 ka. Beyer et al. (2018) found that among six plausible configurations of the San Andreas fault strands, the configuration that includes Galena Peak matches the available geologic slip rates as well as the model without an Active Northern Pathway for slip through the San Gorgonio Pass.

Researchers report differing degrees of recent activity along the Mill Creek and Mission Creek strands west of the Galena Peak strand to the location just west of the A-A' transect within Figure 1. One study of the Mission Creek alluvial complex suggests that neither the Mission Creek nor Mill Creek faults have slipped at this location for 100 ka (site B: Kendrick et al., 2015). In contrast, a sedimentary provenance study of modern drainages just a few kilometers away suggests that the Mission Creek fault may accommodate most of the deformation in the region (Fosdick & Blisniuk, 2018). To the east of the A-A' transect within Figure 1, the Mission Creek strand shows abundant evidence for slip but with a wide range of dextral slip rates. Within the Indio Hills, channel offsets at Pushawalla Canyon show high dextral slip rates of 19.6-23.6 mm/yr over the past ~90 ka (site C: Blisniuk et al., 2021), consistent with active slip along the northern pathway through the SGPr. However, these channels do not record recent slip rates within the past 16 ka. A few kilometers south from Pushawalla Canyon at Three Palms, a young 2.6-6.4 ka alluvial fan shows much lower slip rate of 9-14 mm/yr dextral slip along the Mission Creek strand (site 9: Muñoz Zapata, 2017). A few kilometers north of Pushawalla, offset channels trenched across the Mission Creek fault at Thousand Palms recorded two slip events within the last ~500 years that give slip rates of 2-6 mm/yr (site 8: Fumal et al., 2002). Because trenches can miss expressions of slip along fault splays outside of the trench, we consider this a minimum slip rate for the Thousand Palms site.

The Banning and Mission Creek strands merge into the Coachella segment of the San Andreas fault just south of the Indio Hills (Figure 1). The Coachella segment dips to the northeast (e.g., Fattaruso et al., 2014; Fuis et al., 2017; Lin, 2013; Lindsey & Fialko, 2013) and continues southward from the Indio Hills to the eastern shore of the Salton Sea. Near the Indio Hills, the Mission Creek strand and the Coachella segment dip 5-10 degrees shallower in the Fuis-based models than in the CFM-based models due to changes in the geometry of the Banning strand. This geometry honors the interpretations of Fuis et al. (2017) for the Banning, Garnet Hill and Mission Creek strands to the north of Palm Springs and for the Coachella segment to the south of the Indio Hills. Just south of the junction with the Banning and Mission Creek, the Coachella segment shows evidence from ~50ka alluvial fans for a preferred rate of 14-17 mm/yr at Biskra Palms (site D: Behr et al., 2010).

Site	Name	age	Dextral slip rate (mm/yr)	citation	Used to constrain model slip rate in this study?
1	Cajon Creek	~14 ka	21-28	Weldon & Sieh, 1985	yes
2	Badger Canyon	13-15 ka	$11.8\ ^{+4.2}/_{-3.5}$	McGill et al. 2021	yes
3	Plunge Creek	10.5 ka	6.3-18.5	McGill et al., 2013	yes
A	Wilson Creek	~14 ka	14-25	Harden & Matti, 1989	no; non-robust age
4	Burro Flats	~4 ka	4-12	Orozco et al., 2004	yes
5	Millard Canyon	~8ka	$5.2\ ^{+2.4}/_{-1.4}$	Heermance & Yule, 2017	yes
6	Painted Hills	~6 ka	3.9-4.9	Gold et al., 2015	yes
7	Washington St.	~6 ka	1.5-3.5	Blisniuk et al. 2021	yes
B	Mission Creek Alluvial Fan Complex	>~100ka	0 or > 0	Kendrick et al., 2015; Fosdick & Blisniuk, 2018	not constrained in Active Northern Pathway model
8	Thousand Palms	~500 years	2-6	Fumal et al., 2002	Lower limit
C	Pushawalla Canyon	~90 ka	19.6-23.6	Blisniuk et al. 2021	no; age > 16ka
9	Three Palms	2.6-6.4 ka	9-14	Munoz et al., 2016	yes
D	Biskra Palms	~50ka	14-17	Behr et al., 2010	no; age> 16 ka

Table 1: Data from geologic strike-slip rate sites

Dip slip rates along faults and recent uplift rates are available at only a few locations within the SGPr. In addition to vertical separation of terraces at Millard Canyon (site 5) measured by Heermance et al., (2017), the San Bernardino shows evidence of subsidence. Buried alluvial faults record 1–11.5 mm/yr deposition rates (Carson et al., 1986) and InSAR observations suggest recent subsidence rates of 0.5- 2 mm/yr (Wisely & Schmidt, 2010).

3 Methods

We evaluate the impact of slip rates and sites along faults within the San Gorgonio Pass region (SGPr) using Poly3D, a quasi-static, three-dimensional Boundary Element Method code. Poly3D calculates stresses and displacements throughout the model by solving the linear-elastic equations of continuum mechanics (Crider & Pollard, 1998; Thomas, 1993). To incorporate fault discontinuities within the half-space continuum, Poly3D uses triangular elements built from angular dislocation solution of Comninou and Dundurs (1975). In addition to detailed three-dimensional representation of faults described in section 2, the models incorporate the San Jacinto fault and faults of the Eastern California Shear Zone based on the Community Fault

Model version 5 (Figure 2). Modifications to the Community Fault Model representation have improved the match of model slip rates to geologic slip rates; we include these modifications of the Eastern California Shear Zone described by Herbert et al. (2014) and of the Coachella segment described by Fattaruso et al. (2014). We remeshed the Community Fault Model for more uniform element size and we iteratively refined the mesh to reduce model artifacts that arise when the faults slip.

For the mesh, faults are discretized into triangular elements that can replicate complex fault geometries within a linear-elastic and otherwise homogeneous half-space (Figure 2). Within the SGPr, the average element size is ~4 km, allowing for the models to capture fault irregularities as small as ~10 km. Following Marshall et al. (2009), we extend the faults of the CFM down to a horizontal basal crack that is freely slipping at 35 km depth to simulate distributed deformation below seismogenic depths. This adaptation allows us to simulate long-term deformation without the fault slip rates going to zero at the base of the CFM-defined faults. Furthermore, we do not consider impacts of heterogeneous and/or anisotropic rock properties. Over multiple earthquake cycles, fault geometry provides a first-order control on deformation patterns (e.g., Dawers & Anders, 1995; Fay & Humphreys, 2005; Justin W. Herbert & Cooke, 2012).

Within the unconstrained models, the shear traction-free faults throughout the model slip freely in response to both the tectonic loading and fault interaction. Zero shear traction is consistent with low dynamic strength of faults during rupture (e.g., Goldsby & Tullis, 2011; Di Toro et al., 2006). Tectonic loading is prescribed far from the investigated faults at the base of the model, following Herbert & Cooke (2012) to simulate plate motions that are geodetically constrained as 45-50 mm/yr at 320°-325° (e.g., DeMets et al., 2010). Following Beyer et al. (2018), we also implement an iterative technique that uses a correction ratio for successive iterations to ensure a uniform applied tectonic velocity parallel to the plate boundary (sides labeled I on Figure 2) and a linear gradient in the tectonic loading across the plate boundary (sides labeled II on Figure 2). This technique provides applied velocities that are within ~1% of the desired tectonic loading.

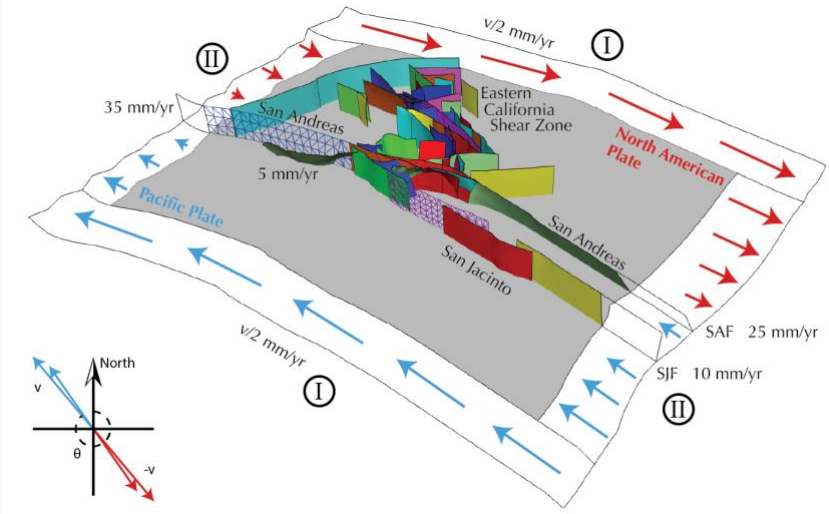

Figure 2. Oblique view of the model setup taken from Beyer et al. (2018). Tectonic loading is prescribed far from the investigated faults at the boundaries of the model base. Zone of applied loading is much wider than shown here. Fault slip rates are prescribed at the distal end of faults that extend beyond the model boundaries. Faults within the model slip freely in response to both tectonic loading and fault interaction. A range of plate velocities and orientations account for uncertainty in tectonic loading. SAF - San Andreas fault; SJF - San Jacinto fault.

To prevent slip from artificially going to zero on faults that extend outside our model area (i.e., the San Andreas, San Jacinto, and Cucamonga-Sierra Madre fault systems), we prescribe slip rates to patches of these faults at the edge of our model. For the San Andreas fault, we apply 35 mm/yr dextral slip (Weldon & Sieh, 1985) at the northwestern edge of the model. At the southeastern edge of the model, we apply 25 mm/yr and 10 mm/yr dextral slip to the San Andreas and San Jacinto faults, respectively (e.g., Becker et al., 2005; Fay & Humphreys, 2005; Meade & Hager, 2005; Sharp, 1981). Deformation within the SGPr is not significantly impacted by variations in the partitioning of slip rates between the San Andreas and San Jacinto faults at this model edge because slip rates primarily respond to interaction among complex faults within the SGPr (Fattaruso et al., 2014). Finally, we apply 1.6 mm/yr reverse slip (McPhillips & Scharer, 2018) to the western edge of the modeled Cucamonga fault to account for deformation along the Sierra Madre fault, which is not included in our model.

Because of the ongoing debate on the recent activity of the Mill Creek strand, we assess two alternative active fault configurations. The first model considers the northern slip pathway inactive through the SGPr; the model does not include the Mill Creek or Galena Peak strands and only allows slip along the Mission Creek strand southeast of the transect A-A' on Figure 1. The second model expands from the first fault configuration and additionally incorporates active Mill Creek and Galena Peak strands as well as the entire Mission Creek strand (Figure 1). We refer to these fault configurations as the *Inactive Northern Pathway* and the *Active Northern Pathway* models.

3.2 Impact of slip rates and their uncertainty

To assess the impact of site specific slip rates and their uncertainty on the fault system we compare the fault slip rates and off-fault deformation of models with both unconstrained and constrained slip rates. Within a first set of unconstrained models, we allow the faults in the model to slip freely in response to tectonic loading and fault interaction. In this first model, the slip rates are mechanically consistent with the fault geometry. For example, if the active fault configuration has a sharp change in fault strike, the slip rate will slow around this kink. However, some of the resulting slip rates may fall outside of the slip rate limits determined from geologic information. In a second set of constrained models, we limit the slip rates at geologic sites within the models to within the geologic range. At each slip rate site along the fault, the prescribed slip rate patch is ~2 km by 2 km, just below the surface trace of the fault. Locations along the faults between the prescribed slip rate sites freely slip in response to tectonic loading, fault interaction, and the effects of prescribed slip patches.

Because geologic investigations produce a range of possible slip rates, we allow for a variety of slip rates at each site of geologic investigation in the model. In the absence of probability density functions for the slip rates, we treat the geologic slip rate as having uniform ("box car') probability within the published range. If the slip rates from the unconstrained model lie outside of the geologic range, then we prescribe the slip rate at the site to be either the upper or lower limit of the geologic slip rate range. If the slip rate in the unconstrained model is closer to the upper bound then we prescribe this slip rate at the site, otherwise we prescribe the lower bound slip rate at the site. Prescribing the geologic slip rate limit honors the geologic observation while also minimizing the deviation from the slip rate that is mechanically consistent with the interpreted active fault geometry (the unconstrained slip rate). In the absence of additional information about local fault geometry, the adjustments to the slip rate at any sites can be considered a proxy for adjusting the local active fault geometry.

Because some sites have uncertain recent slip rates, we either exclude them or limit their role within the constrained models (Table 1). The alluvial fan age at the Wilson Creek (site A) uses qualitative soil chronology rather than modern dating techniques (Harden & Matti, 1989). Because of this uncertainty, we include the slip rate for comparison but do not constrain the model to fit this slip rate. We also exclude slip rate constraints on the Mission Creek strand at the Mission Creek Alluvial Fan Complex (site B) within the *Active Northern Pathway* model because interpretations of recent slip along this portion of the fault (Fosdick & Blisniuk, 2018) do not provide rates. The Kendrick et al. (2015) interpretation of zero slip rate at site B is explicitly considered within the Inactive Northern Pathway model. The slip rate from the Thousand Palms trench (site C) may not include nearby fault strands (Fumal et al., 2002); we use the reported range as only a lower limit for dextral slip rates. Slip rates from the Pushawalla Canyon (site C) and Biskra Palms (sites C) are based on > 60 ka alluvial fans (Behr et al., 2010; Blisniuk et al., 2021). Because the activity among fault strands in the SGPr has shifted over the past 100 ka, strands that were active 60 ka may have different activity now (e.g., Kendrick et al., 2015). Laboratory experiments confirm that restraining bends with greater than 20˚ restraining bend angle, such as the SGPr, are unstable and generate new faults segments (Cooke et al., 2013; Hatem et al., 2015) and slip rates on some bends can vary on time spans of ~50 ka (Elston et al., 2022). Because of the inferred shifts in activity ~100 ka for the SGPr, we only use slip rates from offset of features younger than ~40 ka to constrain the models that simulate current fault slip patterns.

We assess the kinematic incompatibility of the two fault configurations (*Inactive* and *Active Northern Pathway*) for both the unconstrained and constrained models by calculating maps of the off-fault net deformation rate, here defined as the sum of the vorticity rate and the divergence rate derived from the velocity field at the top surface of the model half-space. The vorticity captures the distortion along and off of faults while divergence captures dilatational strain. In order to investigate the off-fault deformation, we exclude net strain rate information within 1 km from all active faults. We compare the resulting off-fault strain rate pattern, the mean strain rate across the region and the uplift pattern to those of the unconstrained models. The spatial patterns

of deformation reveal regions where geologic slip rates are incompatible with interpreted fault geometry, while average net strain rate provides a metric for the relative overall kinematic compatibility of the system. Because the model does not include isostacy, we correct the uplift rates of the model using a model of elastic flexure of the crust that reduces amplitude and increases wavelength of uplift (e.g., Cooke & Dair, 2011; Fattaruso et al., 2014, 2016). Here we use a mantle density of 4500 kg/m^3, crustal density of 2700 kg/m^3, and a flexural rigidity of the crust of 2e23 Pa·m^3.

3.3. Assessing impact of each slip rate site on the system

For the analysis of kinematic compatibility, we constrain the sites so that the models produce slip rates within the geologic bounds. While these results highlight regions of the model where fault geometry is incompatible with geologic slip rates, they do not inform the role of each site on the slip distribution within the system. Due to their structural position, some sites may have a stronger influence on the fault system's slip rate than other sites. We assess the sensitivity of individual sites by exploring the response of the fault system to 1 mm/yr of dextral strike slip applied at each of the sites independently. The influence factors report the change in slip rate at all other sites due to the applied 1 mm/yr at each site. To assess the impact along stretches of fault between the slip rate sites, we also calculate slip rate impact factors by integrating the slip along the fault system that results from applying 1 mm/yr at each site.

4 Results

To assess the roles of fault geometry and slip rate constraints, we present fault slip rates and off-fault deformation through the San Gorgonio Pass region (SGPr) for *Inactive Northern Pathway* and *Active Northern Pathway* models with unconstrained and constrained slip rates. Sites without reliable and young (< 40 ka) slip rates (sites A, B, C and D) are not constrained within the models but are considered within the analysis of site impact. In our assessment of the impact of particular geologic sites on the fault system, we present both the influence of each slip rate site on each other, as well as the regional impact of each slip rate site.

4.1 Surface slip rates through the San Gorgonio Pass region

Forward numerical models that simulate tectonic loading can provide slip rate estimates along the entire fault surface including at the sites of geologic slip rate investigations. Models for the southern San Andreas fault show dextral slip rates at the upper surface of the model that vary along the fault strands through the SGPr (Figures 3a & 3b).

In the model with *Inactive Northern Pathway* geometry (Figure 3a), the dextral slip rate along the San Bernardino strand (maroon) gradually decreases southward from Cajon Pass, with a small, stepped decrease in slip rate between Plunge Creek (site 3) and Wilson Creek (site A), where the San Gorgonio Pass thrust (green) takes up some dextral slip. Dextral slip rate along the San Gorgonio Pass thrust generally increases to the east to reach a maximum of ~6 mm/yr dextral slip near its intersection with the Banning strand (coral). Because strike-slip is partitioned

between both the San Gorgonio Pass thrust and a short active segment of the Banning strand that parallels the San Gorgonio Pass thrust (Fig. 1), the dextral slip rate along the thrust varies along strike. The model produces a local low in dextral slip along the San Gorgonio Pass thrust at Millard Canyon (site 5). Dextral slip on the Garnet Hill strand (beige) decreases to the east, where the fault trace ends just short of reaching the Coachella segment of the San Andreas fault (brown). In contrast, dextral slip on both the Banning strand and the active portion of the Mission Creek strand (purple) increase to the east to maximum values where these faults merge with the Coachella segment.

In the unconstrained *Active Northern Pathway* geometry (Figure 3b), the dextral slip rate along the San Bernardino strand decreases with distance from Cajon Pass, similar to slip rates of the *Inactive Northern Pathway* geometry (Figure 3a). However, unlike the *Inactive Northern Pathway* model, the dextral slip rate abruptly decreases between Badger Canyon (site 2) and Plunge Creek (site 3), due to the transfer of dextral slip onto the Mill Creek strand (blue). Farther to the east, dextral slip of ~10 mm/yr along the Mill Creek strand continues onto the Galena Peak strand (orange). The dextral slip rates along the Mission Creek and Banning strands gradually increase to the southeast where these strands merge with the Coachella segment.

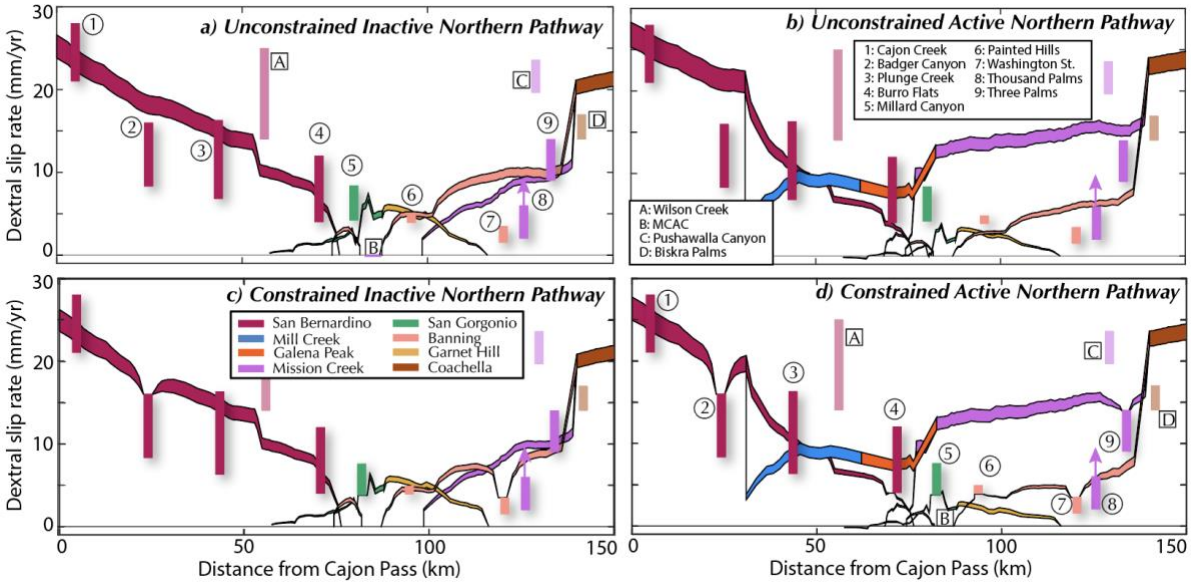

Figure 3. Dextral slip rates along strands of San Andreas fault at the upper surface of the model. Vertical bars show the geologic slip rates at sites labeled in Figure 1; bars with lighter hues are not used for the model assessment. Upward pink arrow indicates that slip rate may exceed the reported range at Thousand Palms. The shaded bands show the range of modeled strike-slip faults for the various applied tectonic loading. a) & b) show results from the unconstrained models with and without an Active Northern Pathway for slip. The *Inactive Northern Pathway* model overlaps more geologic slip rates than the *Active Northern Pathway* model. c) & d) show results for the constrained model where we prescribed strike slip rate to fit within the geologic ranges at sites with robust estimates of slip rate within the past 40 k years.

Model reverse slip rates can be compared with recent reverse slip rates at Millard Canyon (site 5). The *Inactive Northern Pathway* model produces 3.5-6.2 mm/yr and the *Active Northern*

Pathway model produces 3.6-4.5 mm/yr of reverse slip at Millard Canyon. The greater reverse slip of the Inactive Northern Pathway model is consistent with the greater strike-slip along the San Gorgonio Pass thrust along the southern slip pathway. Both reverse rates narrowly exceed the 1.8-3.5 mm/yr range determined by Heermance & Yule (2017) from offset alluvial terraces.

The *Inactive Northern Pathway* model matches more of the geologic strike-slip rates than the *Active Northern Pathway* model (Fig. 3 a & b). Both unconstrained models underestimate strike-slip rates at Millard Canyon (site 5) on the San Gorgonio Pass thrust and the models overestimate slip rates at both Badger Canyon (site 2) and at Washington Street (site 7). While those are the only sites of slip rate mismatch for the *Inactive Northern Pathway* model, the *Active Northern Pathway* model has mismatch at an additional three sites. This model underestimates dextral slip rate at Burro Flats (site 4) and Painted Hills (site 6) and this model overestimates dextral slip rates at Three Palms (site 9). The *Active Northern Pathway* model has much greater dextral slip along the northern pathway and underestimates dextral slip rates at all sites along the southern slip pathway, except for Washington St. (site 7).

In the second pair of models, we constrain the slip rates at sites where rates from the unconstrained models lie outside of the geologic ranges. The slip rates from the constrained models are pinned to the limiting value at sites that did not fall within the range in the unconstrained model. This produces sharp jumps in the dextral slip rate along faults with slip-constrained sites. For both fault configurations (Fig. 3c & d), the San Bernardino strand is pinned to the upper limit of the Badger Canyon slip rate (site 2), the San Gorgonio Pass thrust is pinned to the lower limit of the Millard Canyon dextral slip rate (site 5), and the Banning strand is pinned to the upper limit of the Washington Street slip rate (site 7). Additionally, the *Active Northern Pathway* model has pinned slip rates at the lower limits of the geologic slip rate range along the San Bernardino strand at Burro Flats (site 4) and along the Banning strand at Painted Hills (site 6). The *Active Northern Pathway* model slip rates are also pinned to the upper slip rate limit along the Mission Creek strand at Three Palms (site 9).

The *Active Northern Pathway* model has greater change in slip rate with the imposed constraints than the *Inactive Northern Pathway* model. Integrating the absolute value of change in slip rate along the San Andreas fault within this study area, the *Active Northern Pathway* model has 260 m^2/yr while the *Inactive Northern Pathway* has only 160 m^2/yr of slip rate change. Constraining the slip rates has the greatest impact on slip rate distribution where we have the greatest mismatch between the unconstrained model and the geologic estimates of slip rate. For example, the pinning of slip rates results in slip distribution in the constrained models that differs significantly from both unconstrained models near Washington Street (site 7). The local reduction in slip rate produces sharp gradients in slip rate both east and west of the site in both the *Inactive* and *Active Northern Pathway* models. Local slip rate gradients also arise adjacent to other constrained sites. While the slip rate constraints in the *Active Northern Pathway* model locally impact slip, these constraints do not significantly alter the partitioning of slip between the

northern and southern pathways. The Mission Creek strand maintains ~15 mm/yr of slip and the strands of the southern pathway maintain ~5 mm/yr of dextral slip.

The *Active Northern Pathway* model is not constrained at the Mission Creek alluvial complex (site B) within Figure 3b, even though some studies have found zero slip here along the Mission Creek fault strand (Kendrick, 2015). Figure 4 provides an additional version of the constrained *Active Northern Pathway* model, which adds a constraint of zero dextral slip at the Mission Creek alluvial complex where slip rates are debated (site B). In similar manner as the other sites, constraining slip rate at the Mission Creek alluvial complex produces sharp local gradients in slip rate but does not shift the partitioning of slip rate between the two pathways.

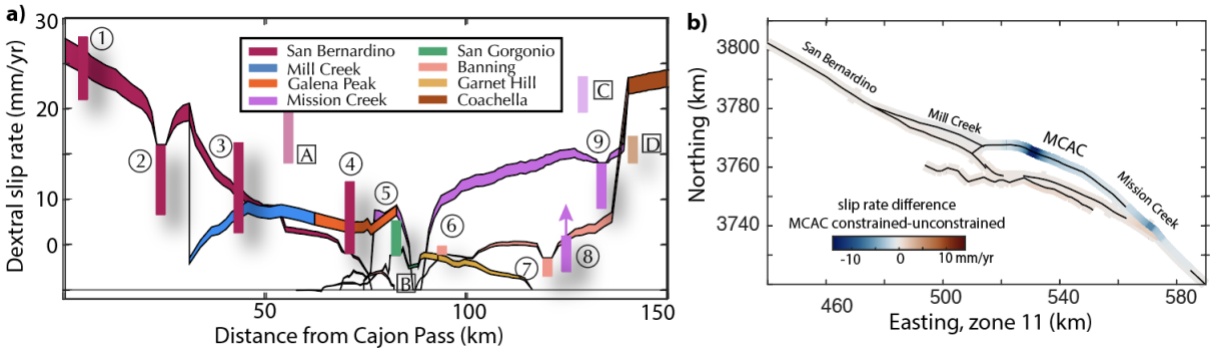

Figure 4. a) Dextral slip rates along strands of San Andreas fault at the upper surface of the model for the constrained *Active Northern Pathway* model of Figure 3d that also limits slip rate to zero at the Mission Creek alluvial complex (MCAC). Vertical bars show the geologic slip rates at sites labeled in Figure 1 - lighter hued bars are slip rates that are not used for the model assessment. b) Difference in slip rate between the constrained *Active Northern Pathway* model of Figure 3d and the model with MCAC also constrained to have zero slip.

4.2 Off-fault deformation

To assess off-fault deformation we sum the vorticity, which produces vertical axis rotation, and the dilation, which produces uplift/subsidence. This net off-fault deformation rate is calculated at distances greater than 1 km from active fault traces (Figure 5). Both models with unconstrained slip produce distributed off-fault deformation within both the western San Bernardino Mountains and the Little San Bernardino Mountains (Figure 5a & 5b). In the unconstrained models of both fault configurations, localized off-fault deformation develops near many fault intersections and irregularities where strike-slip is hindered by these irregularities. Within the *Active Northern Pathway* model, the irregularities along the southern slip pathway produce lesser local off-fault deformation because the southern pathway has lesser dextral slip rate than the *Inactive Northern Pathway* model (Figure 4; Beyer et al., 2018).

The *Inactive Northern Pathway* model produces greater off-fault deformation in the southern San Bernardino Mountains than the *Active Northern Pathway* model. Slip along the additional active fault strands of the northern pathway reduces the local off-fault deformation. Consequently, the mean off-fault deformation calculated >1 km from active faults in the study area decreases with the addition of the northern slip pathway (Table 2). The lower mean off-fault deformation of the

Active Northern Pathway model (83 nanostrain/yr) compared to the *Inactive Northern Pathway* model (87 nanostrain/yr) is consistent with the observation that adding more faults to the system generally allows for greater fault slip and less off-fault deformation (Madden et al., 2017; McBeck et al., 2017).

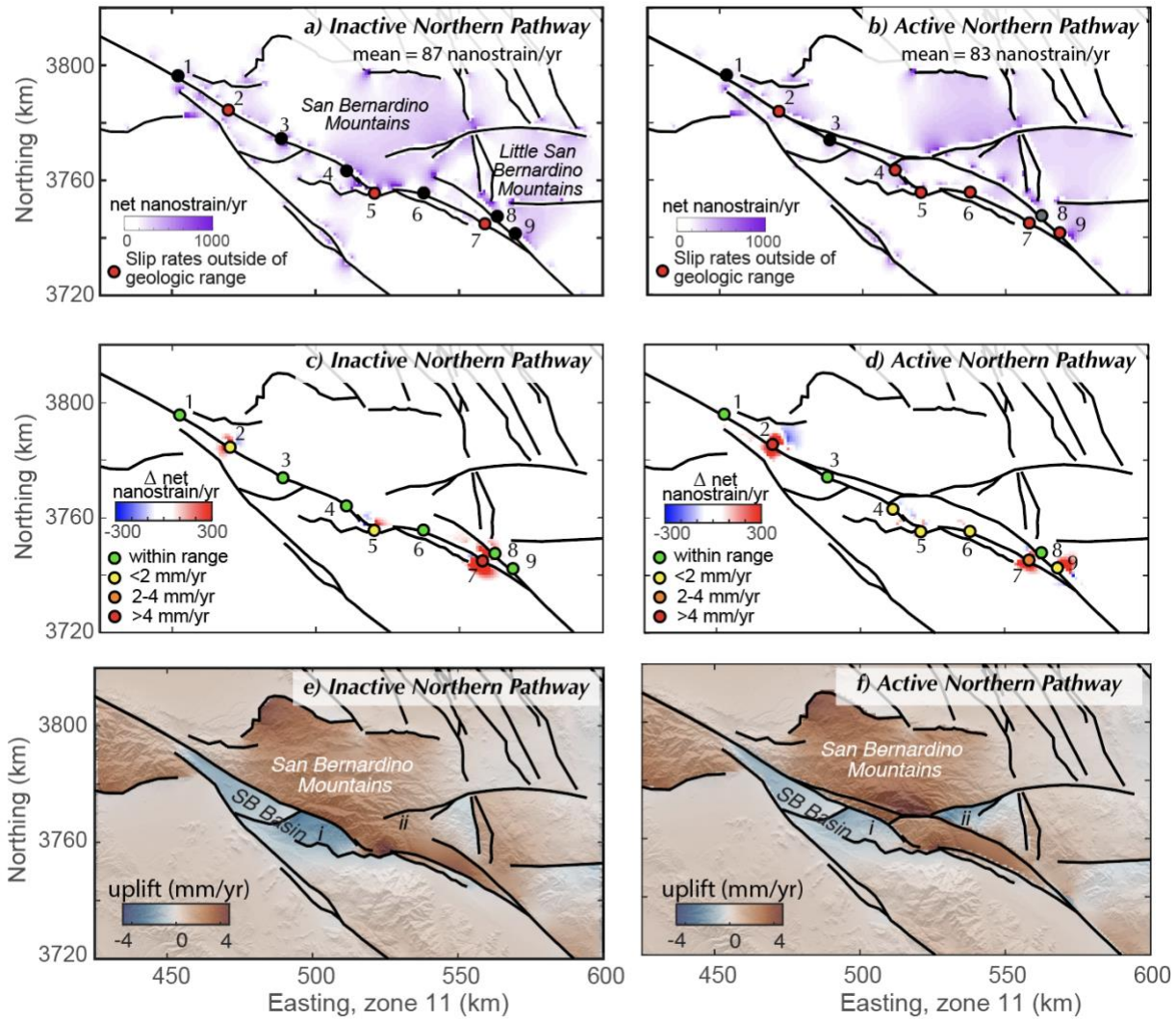

Figure 5. Net off-fault strain maps from *Inactive Northern Pathway* (a&c) and *Active Northern Pathway* (b&d) models, each with tectonic loading at midpoint of the applied range. The top row (a&b) shows strain for the unconstrained models. The middle row (c&d) shows the difference between the unconstrained and the models where slip rates are not permitted to exceed the geologic ranges (constrained-unconstrained). Red indicates regions of increased off-fault deformation when slip rates are constrained for that fault system configuration. The bottom row (e&f) shows the uplift rate pattern, which is due to a combination of off-fault deformation and dip-slip along faults. SB Basin = San Bernardino Basin.

The uplift pattern for both models shows uplift within the San Bernardino mountains consistent with long term rock exhumation patterns. In addition to uplift in regions of net off-fault deformation, dip slip on faults contributes to the uplift pattern. Both models show subsidence in the San Bernardino basin that is consistent with recent measurements (Wisely & Schmidt, 2010). The results highlight several regions where recent uplift data might distinguish between the two plausible models (roman numerals on Figure 5 e&f). The *Inactive Northern Pathway* model predicts greater subsidence at the Banning bench (site i) than the *Active Northern Pathway*. At site ii, east of the Mission Creek Alluvial Complex, the *Inactive Northern Pathway* model predicts uplift while the *Active Northern Pathway* model predicts subsidence. Exposure ages from recent alluvial deposits in these regions may provide valuable constraints to distinguish between the two models.

When we limit the dextral strike-slip rates at sites of the geologic investigations in the models, net off-fault deformation increases near the slip rate sites (Figure 5 c&d). Sites with larger adjustments to their slip rate have greater degree and spatial extent of off-fault deformation (Fig. 5 c&d). For most sites, the off-fault deformation is centered on the site and decreases rapidly with distance. One exception is site 7 (Washington St.) in the *Inactive Northern Pathway* model where the constrained slip rate at this site on the Banning strand impacts off-fault deformation at the nearby Mission Creek strand. Slip on one strand here impacts the other because the faults merge both a few km south of site 7 and also at depth (Figure 1). In the *Active Northern Pathway* model, site 7 does not have as large of a slip rate adjustment as within the *Inactive Northern Pathway* model so this smaller adjustment does not impact off-fault deformation along the Mission Creek strand. The local nature of the changes in off-fault deformation are consistent with the local changes in slip rate distributions near sites with slip rate adjustments (Figure 3).

4.3 Influence of slip rate sites on each other

We map out the influence of slip rates at each site on other sites with a suite of models that apply 1 mm/yr of dextral slip at each slip rate site independently. The tables of Figure 6 b & c show the resulting dextral slip rate detected at each site due to 1 mm/yr dextral slip applied to the sites listed in the first column of the table. Because the Mission Creek alluvial complex (site B) is not part of the *Inactive Northern Pathway* model, it does not have any impact within that model.

The influence of sites varies within the system, and nearby sites have greater influence on each other than distal sites. For example, within both the *Inactive* and *Active Northern Pathway* models, the cluster of sites within the Indio Hills (sites 7-9, C&D) have a large influence on each other (Influence Factor 0.2-0.5; Figure 6 b&c). The influence tables are slightly asymmetric indicating that the influence of slip at one site on another site is not necessarily reciprocal. For example, in the *Active Northern Pathway* model, 1 mm/yr at the Plunge Creek (site 3) produces only 0.06 mm/yr at Badger Canyon (site 2) while 1 mm/yr at Badger Canyon produces 0.10 mm/yr at Plunge Creek. In other words, changes in slip at Badger Canyon have greater influence at Plunge Creek than vice versa in this model. The site influences between the Badger Canyon and Plunge Creek sites are more symmetric in the *Inactive Northern Pathway* model, which

suggests that the presence of the fault branch between Badger Canyon and Plunge Creek in the *Active Northern Pathway* model, reduces the influence of dextral slip at Plunge creek on Badger Canyon. The additional active northern strand also changes the influence of the Wilson Creek (site A) between the *Active* and *Inactive Northern Pathway* models. Most other sites have similar influences on each other between the two models.

The influence of sites on each other generally decreases with distance between sites (Figure 6d). The best fitting exponential curve through the results shows small influence among sites farther than 20 km. In addition to this trend, some sites within 5-20 km of each other have anomalously low and high influence. Three pairs of sites with relatively low influence (1- Burro Flats & Millard Canyon; 2- Mission Creek alluvial complex & Painted Hills; 3- Washington Street & Thousand Palms) are highlighted in blue on Figures 6a and 6d while three pairs of sites with relatively high influence (1 - Cajon Creek & Badger Canyon; 2- Plunge Creek & Wilson Creek; 3- Thousand Palms & Three Palms) are highlighted in red on Figures 6a and 6d. For example, the Badger Canyon and Cajon Creek sites have similar distance (19 km) as the Burro Flats and Painted Hills sites (19 km) but have much larger influence on each other (~0.12 > 0.01). The three pairs of low influence sites for their distances all occur on different segments or parallel branches of the fault system. Even though the sites are nearby one another, slip at one doesn't influence slip on the nearby site because of the lack of fault connectivity at these distances. Pairs of sites on branched faults that are situated very close to the branch, such as Washington Street and Thousand Palms, have influence consistent with the general trend on Figure 6d because slip at one of these sites is close enough to where the faults intersect that slip on one branch can influence the nearby branch. The pairs of sites that have relatively high influence for their distances all occur along continuous portions of the fault without branches, segments, or kinks. Dextral slip transmits more easily along the continuous segments so that slip at one site has a high influence on other sites along the continuous segment.

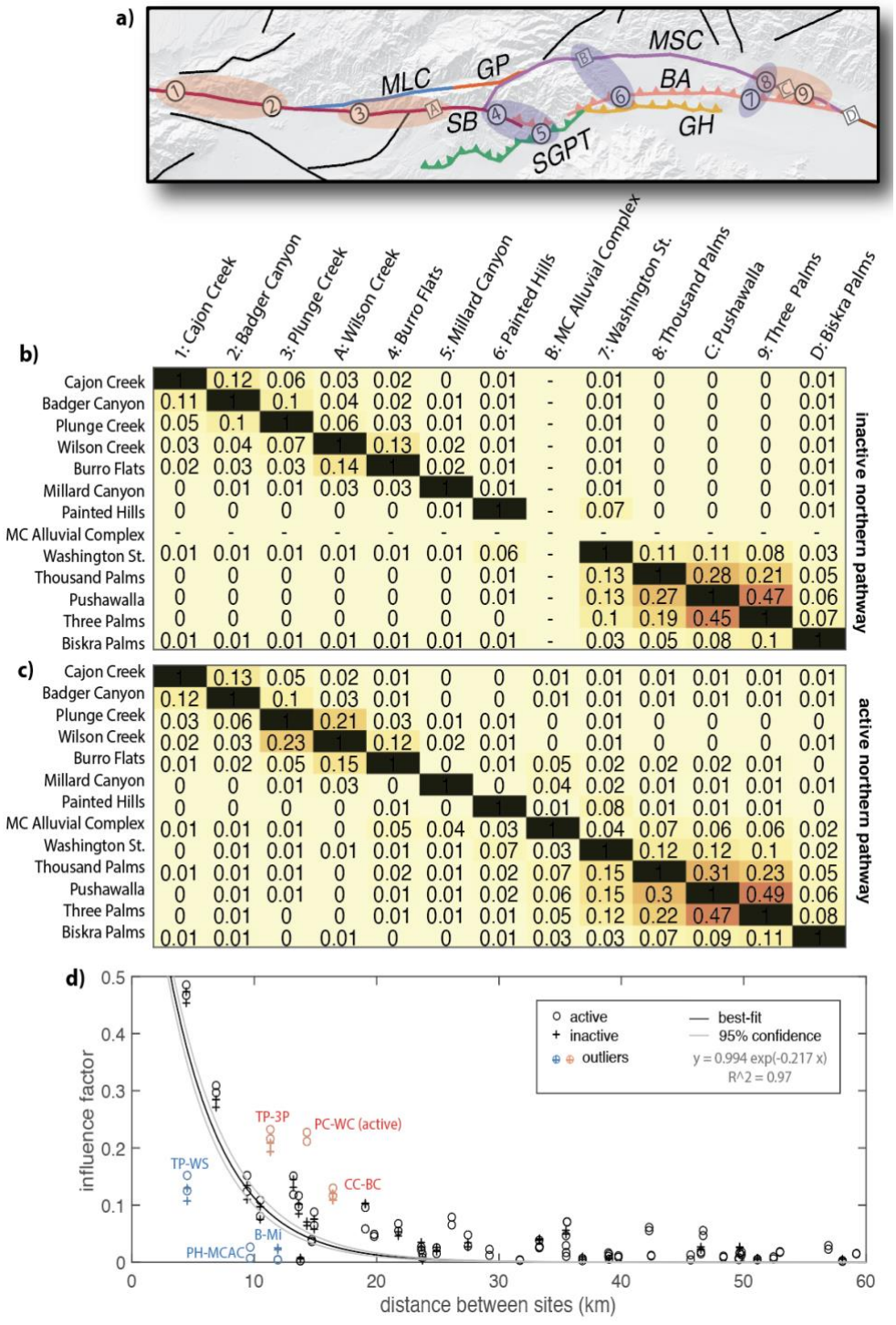

Figure 6. Influence of 1 mm/yr dextral slip applied at sites listed at left on all other sites in the model. a) Map of the site locations with ellipses highlighting pairs of sites with relative high influence (red) and low influence (blue). b) and c) influence for *Inactive Northern Pathway* and *Active Northern Pathway* models respectively. The diagonals of the table are all 1%, reflecting the influence of each site on itself while the off-diagonals show influence values less than one. d) Correlation of influence factor with distance between sites shows that sites have greater influence on nearby sites. Lines show an exponential best fit to all the data. Outliers to the

best fit are highlighted in red and blue. TP - Thousand Palms; 3P- Three Palms; PC - Plunge Creek; WC - Wilson Creek; CC-Cajon Creek; BC- Badger Canyon; WS = Washington Street; PH = Painted Hills; MCAC - Mission Creek Alluvial Complex; B = Burro Flats; Mi = Millard Canyon. MLC = Mill Creek; GP = Galena Peak; SGPT = San Gorgonio Pass Thrust; GH = Garnet Hill; BA = Banning; MSC = Mission Creek.

4.4 Impact of each slip rate site on the fault system

While Figure 6 shows how each site influences slip rate at other sites, that analysis does not inform the impact of the sites' slip rates on the stretches of fault between the sites. To assess this, we map the dextral slip in response to the applied 1 mm/yr at each site and integrate the slip along the faults to derive the total impact factor (Figure 7). The piecewise integration excludes the patch with applied slip and excludes regions with less than 2% of the applied slip (slip < 0.02 mm/yr). In this study, we only constrained slip for the upper 2 km of the fault surface. If these patches were extended to greater depths, we would see greater values for the impact factors among sites and on the system, but the relative impact may be similar.

The *Inactive* and *Active Northern Pathway* models show similar patterns of fault slip for most sites (Figure 7). The impact factors of the sites range from 8 to 25. The lowest impact factor (IF) is at the Millard Canyon site for both model geometries. Sites along the San Bernardino strand in the *Inactive Northern Pathway* model also have relatively low impact factors. The application of 1 mm/yr of slip at these sites produces less fault slip than the other sites, implying that this applied slip produces greater off-fault deformation. For Millard Canyon, off-fault deformation may arise because the site is located within a segmented portion of the southern San Andreas fault, along the San Gorgonio Pass thrust, which does not at the surface meet with the San Bernardino strand. This segmentation leads to greater off-fault deformation in this region.

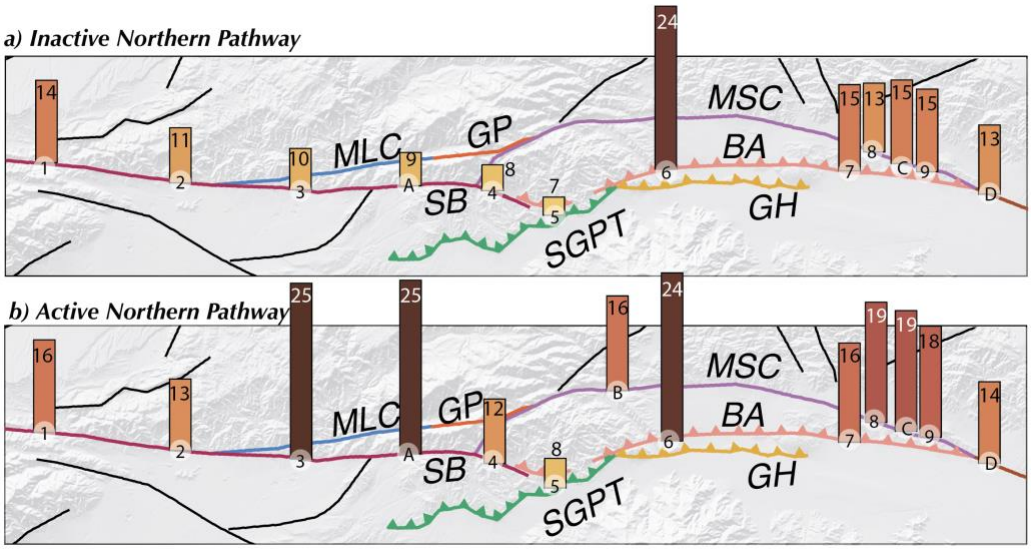

Figure 7. Slip rate impact factors for both the a) *Inactive Northern Pathway* and b) *Active Northern Pathway* models. The darkness and height of the bar represent the impact factor value of each site. MLC = Mill Creek;

GP = Galena Peak; SGPT = San Gorgonio Pass Thrust; GH = Garnet Hill; BA = Banning; MSC = Mission Creek.

The Painted Hills (site 6), which has low influence on other sites (Figure 6) has the greatest impact factor of the sites in the *Inactive Northern Pathway* model (Figure 7). Because this site sits on the Banning strand, which merges with the parallel-striking Garnet Hill strand at depth, slip rates imposed on the Banning strand also impact slip rates on the Garnet Hill strand. The slip distributions plotted on Figure 8 show how slip applied at Painted Hills impacts nearby fault strands. The Garnet Hill strand doesn't yet have any slip rate sites, so the interaction of the Banning and Garnet Hill strands was not considered in the site analysis of Figure 6. The Washington Street (site 7) also occurs along the Banning strand but has a lower impact factor than the Painted Hills site because the Garnet Hill strand is not active as far east as site 7. Furthermore, while the Banning strand merges at depth to the Mission Creek strand at the Washington Street site, these two faults meet much deeper than the Garnet Hill and Banning faults (Figure 1), so the transmission of dextral slip at the Earth's surface is not as efficiently transmitted as between the Banning and Garnet Hills strands at the Painted Hills site.

Due to the longer active fault trace in the *Active Northern Pathway* model, slip from the Washington Street site as well as slip from sites along the Mission Creek strand and Coachella segment extends much farther northwest along the Mission Creek strand than in the *Inactive Northern Pathway* model (Figure 8). This increase in slip extent with the *Active Northern Pathway* model also increases the impact factor of all of the sites.

While most sites increase their impact by 1-3 with the addition of the northern pathway to host dextral slip, the Mission Creek Alluvial Complex and the Plunge Creek and Wilson Creek sites along the San Bernardino strand have impact increases or 15-16. The increase for the Mission Creek Alluvial Complex reflects that this site has zero slip within the *Inactive Northern Pathway* model. For the Plunge Creek and Wilson Creek sites, the close branch angle between the San Bernardino and Mill Creek strands (~10˚) allows dextral slip applied along one branch to produce shear tractions on the other branch that increase the impact factor compared to the model without the branch. Because these sites are within a fault branch in the *Active Northern Pathway* model, they have high impact factor like the Painted Hills site,

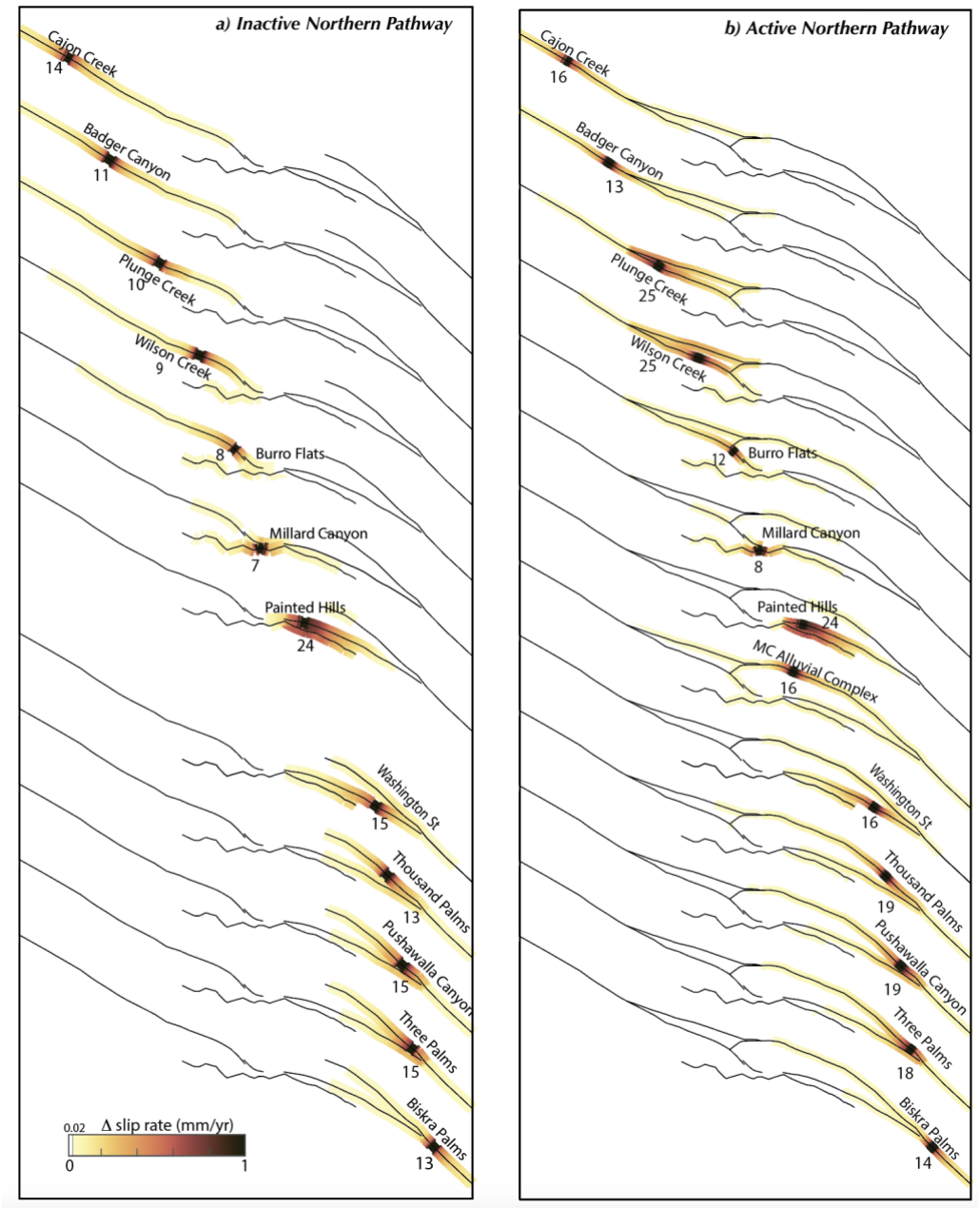

Figure 8. Distribution of dextral slip distribution >2% of the applied slip at each site within the a) *Inactive Northern Pathway* and b) *Active Northern Pathway* models. Numbers report the integrated impact factor along the faults (IF in m^2/yr).

The impact factor of sites along branches is greater than the impact factor of sites outside of the branch (e.g. Badger Canyon) because slip on one branch impacts the other to increase the impact of sites within the branch. For example, in the *Active Northern Pathway* model, the impact factor of the Plunge Creek and Wilson Creek sites is greater than that of the Badger Canyon site, north of the branch of the San Bernardino strand with the Mill Creek Strand. Also in both models, sites along the Mission Creek and Banning strands have greater impact factors than the Biskra Palms site, which is located south of the merger of the Banning and Mission Creek strands.

5 Discussion

Slip rate uncertainties typically derive from the interpretation of offset units (e.g., Cowgill, 2007), offset measurements (e.g., Gold et al., 2009) and the age of materials (e.g., Prush & Oskin, 2020). Studies also show that slip rates can vary over tens of thousands of years, which makes older rates less reliable estimates of current activity. The uncertainties of slip rate estimates can be large enough to permit a variety of active fault geometry interpretations. For example, the *Inactive* and *Active Northern Pathway* models predict dextral slip rates that differ by ~5 mm/yr at Plunge Creek (site #3; Figure 3) south of where the northern and southern pathways branch; however, both model predictions fall within the slip rate uncertainty of McGill et al. (2013). In the face of large uncertainties, collecting slip rate data from additional sites provides one way to constrain active slip partitioning but the results of this study demonstrate that not all sites provide the same impact on our understanding of the active fault system deformation.

5.1 High and low impact structural positions along the fault system

The impact factor of sites depends on structural position and even sites close to each other may have very different impact on the deformation of the fault system (Figure 7). Sites along parallel or subparallel branched fault segments, such as Painted Hills and Plunge Creek sites in the *Active Northern Pathway* model, have greater impact on the fault system than sites outside of the branch because slip is transmitted between connected parallel fault segments. At the same time sites along unconnected strands or near intersecting faults that are not parallel or subparallel, such as Burro Flats and Millard Canyon sites, have low impact factor.

The geologic slip rates typically have uncertainties much larger than the 1 mm/yr applied to the slip rates in the assessment of the sites' impact. Consequently, changes of slip rate within the range of slip rate uncertainty at some sites of geologic slip rate investigation can have a large impact on the partitioning of deformation within the fault system. Along planar strike-slip faults, different sites may have similar impact on the system; however, the complex geometry of the San Andreas fault through the San Gorgonio Pass region produce greatly different slip rate impact with structural position. Slip rate sites along fault branches necessitate detailed consideration because these areas have high impact factors, as slip on one branch impacts slip along the other.

Sites along irregular or disconnected faults have low impact factors and greater nearby off-fault deformation. For example, the Burro Flats and Millard Canyon sites are along relatively disconnected fault strands so that they have both low influence on other sites (Figure 6) and low impact on the nearby fault system (Figures 7&8). The irregular geometry of the San Gorgonio Pass thrust and its connection to the southern end of the San Bernardino strand impedes transmission of dextral slip along the southern slip pathway and contributes to off-fault deformation (Figure 5). The local accumulation of off-fault deformation may promote distributed

inelastic deformation, such as via pressure solution creep (e.g., Gratier et al., 1999) or cleavage development (e.g., Elliott, 1976).

5.2 Incompatibility of slip rates and fault geometry

Where the mechanical model produces slip rates that are consistent with the geologic observations, we confirm that the tested fault geometry is mechanically and kinematically compatible with the slip rates. However, regions where slip rates from the numerical model do not agree with geologic estimates may have incompatibility between the tested fault geometry and slip rate and produce off-fault deformation. In the models with constrained slip rates, this off-fault deformation increases (Figure 5). For both the unconstrained and the constrained models, the *Active Northern Pathway* model produces lesser off-fault deformation than the *Inactive Northern Pathway* model because the addition of the Mill Creek strand provides an additional opportunity for accommodation of strain as fault slip rather than off-fault deformation.

Little to no off-fault deformation occurs where the unconstrained model fault slip rates are within or near the limits of the geologic ranges. The compatibility of dextral slip rates with interpreted fault geometry doesn't preclude the possibility that the models inaccurately represent the subsurface fault configuration. For example, geophysical evidence suggests that rather than the vertical dip represented in this study, the San Bernardino strand may dip to the north east (Fuis et al., 2012). Both vertical and dipping faults can accommodate strike slip so that variations in fault dip might not produce distinguishable dextral slip rates (e.g., Fattaruso et al., 2014).

Regions with mismatched slip rates in both the *Inactive* and *Active Northern Pathway* models (Figure 3), Washington Street (site 7) and Badger Canyon (site 2), indicate that slip rates in these regions may be kinematically incompatible with the interpreted active fault geometry. These incompatibilities highlight the need for additional constraints on subsurface active fault configuration in these regions. While microseismicity during the interseismic period can illuminate subsurface active fault geometry, such as along the San Jacinto fault (Ross et al., 2017), the southern San Andreas fault has not produced much microseismicity during the recorded catalog. Uncertainty persists on the subsurface geometry of active faults in these regions. For example, at Cajon Pass, the San Andreas and San Jacinto faults may be connected at depth even though the surface traces are separated by several km (e.g., Matti & Morton, 1993; McGill et al., 2013). A hard connection at depth between these faults would alter slip distribution among the faults. Mechanical models of Herbert et al. (2014) show that connecting the San Jacinto and San Andreas faults reduces dextral slip rates at the Badger Canyon (site 2), which would better match the site's geologic slip rates.

Near the Indio Hills, the Banning and Mission Creek strands merge into the Coachella segment of the San Andreas fault. The subsurface geometry of the faults near this intersection is not well constrained (e.g., Fuis et al., 2017). The off-fault deformation in this region and the mismatch to geologic slip estimates (Figure 5) could be a result of incorrectly inferred fault geometry. For example, while the Garnet Hill strand does not produce surface expression of active faulting, it

may connect to the Coachella at depth. If the models included such a connection, the Garnet Hill strain might take up dextral slip currently partitioned to the Banning strand and reduce the slip rate.

5.3 Potential data to assess activity along northern slip pathway

The results of this study and that of Beyer et al. (2018) show that adding a northern pathway for fault slip modifies slip distribution. While it is agreed that the Mission Creek strand is active near its intersection with the Banning strand, debate persists on the activity of the northern pathway near and northwest of the Mission Creek alluvial complex (Beyer et al., 2018; Fosdick & Blisniuk, 2018; Kendrick et al., 2015). This study is not able to ascertain between the two viable models, but it does highlight areas where additional geologic data may provide critical evidence for the partitioning of slip along faults. We need recent geologic data to resolve the ongoing debate about activity along the northern strand of the San Andreas fault. Because the northern pathway was active > 100 ka, we need young ages to resolve current activity (Kendrick et al., 2015). Furthermore, the region's complex history provides several potential slip surfaces so that low slip rate along one fault does not preclude another nearby fault accommodating dextral slip along a northern pathway. Nevertheless, we can benefit from additional slip rates from the various faults along the Northern Pathway.

Slip along the northern pathway also impacts deformation in the region that can be used to delineate between the plausible active fault models. The Wilson Creek site (#4) has slip rates that differ by 5 mm/yr between the *Inactive* and *Active Northern Pathway* models. Because the age of the alluvial fan was estimated from soil chronology (Harden & Matti, 1989) rather than modern dating techniques, redating of this surface might provide substantial improvement to our understanding of strain partitioning and potential activity of the northern pathway. Additionally, uplift rates from the region between the Pinto Mountain fault and the Mission Creek strand (region labeled ii on Figure 5) could distinguish between the models. The model predicts uplift if the northern pathway is inactive and subsidence if the norther pathway is active. Such additional geologic data would be valuable for resolving the ongoing debate about activity along the northern strand of the San Andreas fault.

The two alternative models also predict differing degrees of off-fault deformation between the southern and northern pathways (Figure 5); the *Active Northern Pathway* produces negligible off-fault deformation between the pathways while the *Inactive Northern Pathway* model produces ~500 nanstrain/yr. However, documenting recent off-fault deformation rates can be challenging. The catalog of microseismicity in this region may indicate significant secondary deformation (e.g, slip along existing surfaces), but this deformation may vary through the earthquake cycle and might not represent long-term strain partitioning. Furthermore, the lack of microseismicity does not confirm lack of strain accumulation. Current off-fault deformation rates are difficult to constrain with geologic data. Most methods of estimating off-fault deformation rates, such as paleomagnetic records of vertical axis rotation (e.g., Titus et al., 2011) and folding of contracted units (e.g., Scharer et al., 2004), are generally not available for young unlithified

sediments. Data collected from units older than 100 ka need to consider the variation in fault activity in the region (Fattaruso et al., 2016), which complicates the delineation of current fault activity.

5.4 Seismic hazard

The numerical models demonstrate the high spatial variability of strike-slip rates along faults with non-planar configuration. The southern San Andreas fault is one of the most thoroughly investigated fault systems in the world; most restraining bends and branches along strike-slip faults have far fewer slip rate data than this fault system. If seismic hazard estimates use a single rate to represent slip rates through a complex restraining bend, they might miss the spatial variations of strike-slip rate. Strike-slip fault branches show particularly high spatial variability of slip rate (Figure 3), accrual of nearby off-fault deformation (Figure 5) and impact on the fault system (Figures 7 and 8). Fault branches warrant detailed investigation in order to best understand regional strain partitioning. Furthermore, the range of impact factors for the different sites demonstrates that not all slip rate sites have equal impact. Consequently, if we have errors or are off in our estimate of slip rate at any one of the more sensitive sites, this error may have a large impact on our understanding of the deformation of the fault system and thus hinder our ability to accurately assess seismic hazard in the region.

7 Conclusions

We use three-dimensional numerical crustal deformation models to analyze the role of slip rate sites in determining deformation of the southern San Andreas fault system within the San Gorgonio Pass region. We investigate the compatibility of models with and without active slip along the northern pathway of the San Andreas fault around the San Gorgonio Pass region with geologic slip rates. Within unconstrained models that allow all faults to slip freely everywhere in response to tectonic loading and fault interaction, the *Active Northern Pathway* model produces slip rates with greater mismatch to young (<40 ka) rates at sites of geologic investigations than the *Inactive Northern Pathway* model. To assess incompatibilities between fault geometry and slip rate, we utilize a new approach and constrain the slip rates along the faults to within the geologic range at each geologic slip rate site. Slip rate adjustments in the constrained model ensure that the model matches all geologic slip rates, but this produces local off-fault deformation near the constrained sites.

Maps of off-fault deformation show that the *Inactive Northern Pathway* fault configuration for both the unconstrained and the constrained models has greater off-fault deformation than the *Active Northern Pathway*. The additional northern slip pathway provides an opportunity for a greater amount of deformation to be expressed as fault slip. While fault systems may evolve to reach more efficient configurations (e.g., Hatem et al., 2017; McBeck et al., 2017), this does not mean that the presently active configuration must be the most optimal. Additional slip rate constraints and data off-fault deformation rates within the southern San Andreas system would provide valuable information to assess between the two alternative configurations.

We assess how much of an impact the incompatibilities between fault geometry and geologic slip rate have on the system by assessing the impact of slip rate changes. Small changes of slip rate at any one site of geologic slip rate investigation impact slip rates elsewhere in the system. However, this impact is not the same for all sites, which means that inaccuracies in the slip rate that we use for seismic hazard analysis may have differing impact along active fault systems at one site than another. The degree of impact that slip rate sites have on the fault system depends on their structural positions. Sites along segmented faults may have lesser impact than sites along a continuous fault segment, and sites along fault branches have the greatest impact. Fault branches along strike-slip faults require detailed investigation because these areas have high spatial variability of slip rate and can impact the nearby branches of the fault system, adding additional uncertainty to our current assessment of the seismic hazard.

Acknowledgements

This research was partially supported by the Southern California Earthquake Center (Contribution No. 11878). SCEC is funded by NSF Cooperative Agreement EAR-1600087 & USGS Cooperative Agreement G17AC00047. The authors thank Nicolas Harrichhausen, Wenbin Xu and an anonymous reviewer for their suggestion on a previous version of this manuscript submitted to Seismica.

Data and code availability

The crustal deformation software Poly3D is made available by the Stanford Tectonic Geomorphology lab at https://github.com/stgl/poly3d. Input files for the unconstrained and constrained Active Northern Pathway and Inactive Northern Pathway models used in this study can be downloaded from doi:10.6084/m9.figshare.20274363

Competing interests

The authors have no competing interests.

References

Becker, T. W., Hardebeck, J. L., & Anderson, G. (2005). Constraints on fault slip rates of the southern California plate boundary from GPS velocity and stress inversions. *Geophysical Journal International, 160*(2), 634–650. https://doi.org/10.1111/j.1365-246X.2004.02528.x

Behr, W. M., Rood, D. H., Fletcher, K. E., Guzman, N., Finkel, R., Hanks, T. C., et al. (2010). Uncertainties in slip-rate estimates for the Mission Creek strand of the southern San Andreas fault at Biskra Palms Oasis, southern California. *Bulletin of the Geological Society of America, 122*(9–10), 1360–1377. https://doi.org/10.1130/B30020.1

Beyer, J. L., Cooke, M. L., & Marshall, S. T. (2018). Sensitivity of deformation to activity along the Mill Creek and Mission Creek strands of the southern San Andreas fault. *Geosphere, 14*(6), 2296–2310. https://doi.org/10.1130/GES01666.1

Blisniuk, K., Scharer, K., Sharp, W. D., Burgmann, R., Amos, C., & Rymer, M. (2021). A revised position for the primary strand of the Pleistocene-Holocene San Andreas fault in southern California. *Science Advances*, *7*(13). https://doi.org/10.1126/sciadv.aaz5691

Carson, S. E., Matti, J. C., Throckmorton, C. K., & Kelly, M. M. (1986). *Stratigraphic and geotechnical data from a regional drilling investigation in the San Bernardino Valley, California*. US Geological Survey,.

Comninou, M., & Dundurs, J. (1975). The angular dislocation in a half space. *Journal of Elasticity*, *5*(3), 203–216.

Cooke, M. L., & Dair, L. C. (2011). Simulating the recent evolution of the southern big bend of the San Andreas fault, Southern California. *Journal of Geophysical Research: Solid Earth*, *116*(4). https://doi.org/10.1029/2010JB007835

Cooke, M. L., Schottenfeld, M. T., & Buchanan, S. W. (2013). Evolution of fault efficiency at restraining bends within wet kaolin analog experiments. *Journal of Structural Geology*, *51*, 180–192. https://doi.org/10.1016/j.jsg.2013.01.010

Cooke, M. L., Toeneboehn, K., & Hatch, J. L. (2020). Onset of slip partitioning under oblique convergence within scaled physical experiments. *Geosphere*, *16*(X), 1–15. https://doi.org/10.1130/ges02179.1

Cowgill, E. (2007). Impact of riser reconstructions on estimation of secular variation in rates of strike–slip faulting: Revisiting the Cherchen River site along the Altyn Tagh Fault, NW China. *Earth and Planetary Science Letters*, *254*(3–4), 239–255.

Crider, J. G., & Pollard, D. D. (1998). Fault linkage: Three-dimensional mechanical interaction between echelon normal faults. *Journal of Geophysical Research*, *103391*(10), 373–24. https://doi.org/10.1029/98JB01353

Dawers, N. H., & Anders, M. H. (1995). Displacement-length scaling and fault linkage. *Journal of Structural Geology*, *17*(5), 607–614.

DeMets, C., Gordon, R. G., & Argus, D. F. (2010). Geologically current plate motions. *Geophysical Journal International*, *181*(1), 1–80. https://doi.org/10.1111/j.1365-246X.2009.04491.x

Dibblee, T. W. (1964). *Geologic map of the San Gorgonio Mountain quadrangle, San Bernardino and Riverside Counties, California*. US Geological Survey.

Elliott, D. (1976). The Energy Balance and Deformation Mechanisms of Thrust Sheets Philosophical Transactions of the Royal Society of London . Series A , Mathematical and Physical Sciences , Vol . 283 , No . 1312 , A Discussion on Natural Strain and Geological Structure . (. *Strain*, *283*(1312), 289–312.

Elston, H., Cooke, M., & Hatem, A. (2022). Non-steady-state slip rates emerge along evolving restraining bends under constant loading. *Geology*, *50*(5), 532–536. https://doi.org/10.1130/G49745.1

Fattaruso, L. A., Cooke, M. L., & Dorsey, R. J. (2014). Sensitivity of uplift patterns to dip of the San Andreas fault in the Coachella Valley, California. *Geosphere*, *10*(6). https://doi.org/10.1130/GES01050.1

Fattaruso, L. A., Cooke, M. L., Dorsey, R. J., & Housen, B. A. (2016). Response of deformation patterns to reorganization of the southern San Andreas fault system since ca. 1.5ï¿½Ma. *Tectonophysics*, *693*, 474–488. https://doi.org/10.1016/j.tecto.2016.05.035

Fay, N. P., & Humphreys, E. D. (2005). Fault slip rates, effects of elastic heterogeneity on geodetic data, and the strength of the lower crust in the Salton Trough region, southern California. *Journal of Geophysical Research: Solid Earth*, *110*(9), 1–14. https://doi.org/10.1029/2004JB003548

Fosdick, J. C., & Blisniuk, K. (2018). Sedimentary signals of recent faulting along an old strand of the San Andreas Fault, USA. *Scientific Reports*, *8*(1), 12132.

Fuis, G. S., Scheirer, D. S., Langenheim, V. E., & Kohler, M. D. (2012). A new perspective on the Geometry of the San Andreas fault in southern California and its relationship to Lithospheric structure. *Bulletin of the Seismological Society of America*, *102*(1), 236–251. https://doi.org/10.1785/0120110041

Fuis, G. S., Bauer, K., Goldman, M. R., Ryberg, T., Langenheim, V. E., Scheirer, D. S., et al. (2017). Subsurface geometry of the san andreas fault in southern California: Results from the salton seismic imaging project (SSIP) and strong ground motion expectations. *Bulletin of the Seismological Society of America*, *107*(4), 1642–1662. https://doi.org/10.1785/0120160309

Fumal, T. E., Rymer, M. J., & Seitz, G. G. (2002). Timing of large earthquakes since A.D. 800 on the Mission Creek strand of the San Andreas fault zone at Thousand Palms Oasis, near Palm Springs, California. *Bulletin of the Seismological Society of America*, *92*(7), 2841–2860. https://doi.org/10.1785/0120000609

Gabrielov, A., Keilis-Borok, V., & Jackson, D. D. (1996). Geometric incompatibility in a fault system. *Proceedings of the National Academy of Sciences of the United States of America*, *93*(9), 3838–3842. https://doi.org/10.1073/pnas.93.9.3838

Gold, P. O., Behr, W. M., Rood, D., Sharp, W. D., Rockwell, T. K., Kendrick, K., & Salin, A. (2015). Holocene geologic slip rate for the Banning strand of the southern San Andreas Fault, southern California. *Journal of Geophysical Research: Solid Earth*, *120*(8), 5639–5663.

Gold, R. D., Cowgill, E., Arrowsmith, J. R., Gosse, J., Chen, X., & Wang, X. (2009). Riser diachroneity, lateral erosion, and uncertainty in rates of strike-slip faulting: A case study from Tuzidun along the Altyn Tagh Fault, NW China. *Journal of Geophysical Research: Solid Earth*, *114*(B4).

Goldsby, D. L., & Tullis, T. E. (2011). Flash heating leads to low frictional strength of crustal rocks at earthquake slip rates. *Science*, *334*(6053), 216–218.

Gratier, J.-P., Renard, F., & Labaume, P. (1999). How pressure solution creep and fracturing processes interact in the upper crust to make it behave in both a brittle and viscous manner. *Journal of Structural Geology*, *21*(8–9), 1189–1197.

Harden, J., & Matti, J. (1989). Holocene and late Pleistocene slip rates on the San Andreas fault in Yucaipa, California, using …. *Bulletin of the Geological Society of America*, (September), 1107–1117. https://doi.org/10.1130/0016-7606(1989)101<1107

Hatem, A. E., Cooke, M. L., & Madden, E. H. (2015). Evolving efficiency of restraining bends within wet kaolin analog experiments. *Journal of Geophysical Research: Solid Earth, 120*(3), 1975–1992. https://doi.org/10.1002/2014JB011735

Hatem, A. E., Cooke, M. L., & Toeneboehn, K. (2017). Strain localization and evolving kinematic efficiency of initiating strike-slip faults within wet kaolin experiments. *Journal of Structural Geology, 101*. https://doi.org/10.1016/j.jsg.2017.06.011

Heermance, R. V., & Yule, D. (2017). Holocene slip rates along the San Andreas Fault System in the San Gorgonio Pass and implications for large earthquakes in southern California. *Geophysical Research Letters, 44*(11), 5391–5400. https://doi.org/10.1002/2017GL072612

Herbert, J.W., Cooke, M. L., & Marshall, S. T. (2014). Influence of fault connectivity on slip rates in southern California: Potential impact on discrepancies between geodetic derived and geologic slip rates. *Journal of Geophysical Research: Solid Earth, 119*(3). https://doi.org/10.1002/2013JB010472

Herbert, Justin W., & Cooke, M. L. (2012). Sensitivity of the Southern San Andreas fault system to tectonic boundary conditions and fault configurations. *Bulletin of the Seismological Society of America, 102*(5). https://doi.org/10.1785/0120110316

Kendrick, K. J., Matti, J. C., & Mahan, S. A. (2015). Late quaternary slip history of the Mill Creek strand of the San Andreas fault in San Gorgonio Pass, southern California: The role of a subsidiary left-lateral fault in strand switching. *Bulletin of the Geological Society of America, 127*(5–6), 825–849. https://doi.org/10.1130/B31101.1

Lin, G. (2013). Three-dimensional seismic velocity structure and precise earthquake relocations in the Salton trough, southern California. *Bulletin of the Seismological Society of America, 103*(5), 2694–2708.

Lindsey, E. O., & Fialko, Y. (2013). Geodetic slip rates in the southern San Andreas Fault system: Effects of elastic heterogeneity and fault geometry. *Journal of Geophysical Research: Solid Earth, 118*(2), 689–697. https://doi.org/10.1029/2012JB009358

Madden, E. H., Cooke, M. L., & McBeck, J. A. (2017). Energy budget and propagation of faults via shearing and opening using work optimization. *Journal of Geophysical Research: Solid Earth, 122*(8), 6757–6772. https://doi.org/10.1002/2017JB014237

Marshall, S. T., Cooke, M. L., & Owen, S. E. (2009). Interseismic deformation associated with three-dimensional faults in the greater Los Angeles region, California. *Journal of Geophysical Research: Solid Earth, 114*(12). https://doi.org/10.1029/2009JB006439

Matti, J. C., & Morton, D. M. (1993). Paleogeographic evolution of the San Andreas fault in southern California: A reconstruction based on a new cross-fault correlation. *The San Andreas Fault System: Displacement, Palinspastic Reconstruction, and Geologic Evolution*, 107–159. https://doi.org/10.1130/MEM178-p107

Matti, J. C., Morton, D. M., & Cox, B. F. (1985). *Distribution and geologic relations of fault systems in the vicinity of the central Transverse Ranges, southern California*. US Geological Survey.

McBeck, J. A., Cooke, M. L., Herbert, J. W., Maillot, B., & Souloumiac, P. (2017). Work

Optimization Predicts Accretionary Faulting: An Integration of Physical and Numerical Experiments. *Journal of Geophysical Research: Solid Earth*, *122*(9), 7485–7505. https://doi.org/10.1002/2017JB013931

McGill, S. F., Owen, L. A., Weldon, R. J., & Kendrick, K. J. (2013). Latest pleistocene and holocene slip rate for the San Bernardino Strand of the San Andreas Fault, Plunge Creek, Southern California: Implications for strain partitioning within the Southern San Andreas Fault system for the last ~35 k.y. *Bulletin of the Geological Society of America*, *125*(1–2), 48–72. https://doi.org/10.1130/B30647.1

McGill, S. F., Owen, L. A., Weldon, R. J., Kendrick, K. J., & Burgette, R. J. (2021). Latest Quaternary slip rates of the San Bernardino strand of the San Andreas fault, southern California, from Cajon Creek to Badger Canyon. *Geosphere*, *17*(5), 1354–1381. https://doi.org/10.1130/GES02231.1

McPhillips, D., & Scharer, K. M. (2018). Quantifying Uncertainty in Cumulative Surface Slip Along the Cucamonga Fault, a Crustal Thrust Fault in Southern California. *Journal of Geophysical Research: Solid Earth*, *123*(10), 9063–9083. https://doi.org/10.1029/2018JB016301

Meade, B. J., & Hager, B. H. (2005). Block models of crustal motion in southern California constrained by GPS measurements. *Journal of Geophysical Research: Solid Earth*, *110*(3), 1–19. https://doi.org/10.1029/2004JB003209

Muñoz Zapata, J. J. (2017). Holocene geologic slip rate for the Mission Creek strand of the southern San Andreas fault, Indio Hills.

Orozco, A. A. (2004). Offset of a mid-Holocene alluvial fan near Banning, CA: Constraints on the slip rate of the San Bernardino strand of the San Andreas Fault. California State University, Northridge.

Plesch, A., Shaw, J. H., Benson, C., Bryant, W. A., Carena, S., Cooke, M., et al. (2007). Community Fault Model (CFM) for southern California. *Bulletin of the Seismological Society of America*, *97*(6). https://doi.org/10.1785/0120050211

Plesch, A., Shaw, J. H., & Kronman, D. (2007). Mechanics of low-relief detachment folding in the Bajiaochang field, Sichuan Basin, China. *AAPG Bulletin*, *91*(11), 1559–1575. https://doi.org/10.1306/06200706072

Prush, V. B., & Oskin, M. E. (2020). A mechanistic erosion model for cosmogenic nuclide inheritance in single-clast exposure ages. *Earth and Planetary Science Letters*, *535*, 116066.

Ross, Z. E., Hauksson, E., & Ben-Zion, Y. (2017). Abundant off-fault seismicity and orthogonal structures in the San Jacinto fault zone. *Science Advances*, *3*(3). https://doi.org/10.1126/sciadv.1601946

Scharer, K. M., Burbank, D. W., Chen, J., Weldon, R. J., Rubin, C., Zhao, R., & Shen, J. (2004). Detachment folding in the Southwestern Tian Shan–Tarim foreland, China: shortening estimates and rates. *Journal of Structural Geology*, *26*(11), 2119–2137.

Sharp, R. V. (1981). Variable rates of late Quaternary strike slip on the San Jacinto fault zone, southern California. *Journal of Geophysical Research*, *86*(B3), 1754–1762.

https://doi.org/10.1029/JB086iB03p01754

Shaw, J. H., Plesch, A., Tape, C., Suess, M. P., Jordan, T. H., Ely, G., et al. (2015). Unified structural representation of the southern California crust and upper mantle. *Earth and Planetary Science Letters*, *415*, 1–15.

Stanford tectonic geomorphology lab. (n.d.). Poly3D. Retrieved from https://github.com/stgl/poly3d

Thomas, A. (1993). Poly3D: A three-dimensional, polygonal element, displacement boundary element computer program with applications to fractures, faults, and cavities in the Earth's crust [MS thesis].

Titus, S. J., Crump, S., McGuire, Z., Horsman, E., & Housen, B. (2011). Using vertical axis rotations to characterize off-fault deformation across the san andreas fault system, central California. *Geology*, *39*(8), 711–714. https://doi.org/10.1130/G31802.1

Di Toro, G., Hirose, T., Nielsen, S. B., & Pennacchioni, G. (2006). Natural and Experimental Evidence During Earthquakes, *311*(February), 647–649.

Weldon, R. J., & Sieh, K. E. (1985). Holocene rate of slip and tentative recurrence interval for large earthquakes of the San Andreas fault, Cajon Pass, southern California. *Geological Society of America Bulletin*, *96*(6), 793–812. https://doi.org/10.1130/0016-7606(1985)96<793:HROSAT>2.0.CO;2

Wisely, B. A., & Schmidt, D. (2010). Deciphering vertical deformation and poroelastic parameters in a tectonically active fault-bound aquifer using InSAR and well level data, San Bernardino basin, California. *Geophysical Journal International*, *181*(3), 1185–1200. https://doi.org/10.1111/j.1365-246X.2010.04568.x

Yule, D., & Sieh, K. (2003). Complexities of the San Andreas fault near San Gorgonio Pass: Implications for large earthquakes. *Journal of Geophysical Research*, *108*(B11), 2548. https://doi.org/10.1029/2001JB000451